Article:

Salcedo Hernandez, Y., Newman, J.A., Andrews, B.H. et al. (2026) Highly efficient selection of high-redshift emission-line galaxies for future DESI-like surveys with deep multiband imaging. The Astronomical Journal, 172 (1). 11. ISSN: 0004-6256

https://doi.org/10.3847/1538-3881/ae6b7c

The Astronomical Journal, 172:11 (15pp), 2026 July https://doi.org/10.3847/1538-3881/ae6b7c

Highly Efficient Selection of High-redshift Emission-line Galaxies for Future DESI-like Surveys with Deep Multiband Imaging

Yoquelbin Salcedo Hernandez[1,2], Jeffrey A. Newman[1,2], Brett H. Andrews[1,2], B. Dey[1,2,3], R. Zhou[4], N. Sailer[4,5,6,7], J. Aguilar[4], S. Ahlen[8], D. Bianchi[9,10], D. Brooks[11], R. Canning[12], F. J. Castander[13,14], E. Chaussidon[4], T. Claybaugh[4], A. Cuceu[4], A. de la Macorra[15], A. Dey[16], P. Doel[11], S. Ferraro[4,7], A. Font-Ribera[17,18], J. E. Forero-Romero[19,20], E. Gaztañaga[12,13,14], S. Gontcho A Gontcho[21], G. Gutierrez[22], H. K. Herrera-Alcantar[23,24], R. Joyce[16], S. Juneau[16], R. Kehoe[25], D. Kirkby[26], T. Kisner[4], A. Kremin[4], O. Lahav[11], C. Lamman[27], M. Landriau[4], M. E. Levi[4], M. Manera[18,28], A. Meisner[16], R. Miquel[17,18], J. Moustakas[29], S. Nadathur[12], N. Palanque-Delabrouille[4,24], W. J. Percival[30,31,32], F. Prada[33], I. Pérez-Ràfols[34], A. Raichoor[4], G. Rossi[35], E. Sanchez[36], D. Schlegel[4], M. Schubnell[37,38], H. Seo[39], J. Silber[4], D. Sprayberry[16], G. Tarlé[38], B. A. Weaver[16], C. Yèche[24], and H. Zou[40]

[1] Department of Physics & Astronomy and Pittsburgh Particle Physics, Astrophysics, and Cosmology Center (PITT PACC), University of Pittsburgh, 3941 O'Hara Street, Pittsburgh, PA 15260, USA
[2] Pittsburgh Particle Physics, Astrophysics, and Cosmology Center (PITT PACC), University of Pittsburgh, Pittsburgh, PA 15260, USA
[3] Department of Astronomy & Astrophysics, University of Toronto, Toronto, ON M5S 3H4, Canada
[4] Lawrence Berkeley National Laboratory, 1 Cyclotron Road, Berkeley, CA 94720, USA
[5] Kavli Institute for Particle Astrophysics and Cosmology, 382 Via Pueblo Mall, Stanford, CA 94305, USA
[6] SLAC National Accelerator Laboratory, 2575 Sand Hill Road, Menlo Park, CA 94025, USA
[7] University of California, Berkeley, 110 Sproul Hall #5800 Berkeley, CA 94720, USA
[8] Department of Physics, Boston University, 590 Commonwealth Avenue, Boston, MA 02215, USA
[9] Dipartimento di Fisica "Aldo Pontremoli," Università degli Studi di Milano, Via Celoria 16, I-20133 Milano, Italy
[10] INAF-Osservatorio Astronomico di Brera, Via Brera 28, 20122 Milano, Italy
[11] Department of Physics & Astronomy, University College London, Gower Street, London, WC1E 6BT, UK
[12] Institute of Cosmology and Gravitation, University of Portsmouth, Dennis Sciama Building, Portsmouth, PO1 3FX, UK
[13] Institut d'Estudis Espacials de Catalunya (IEEC), c/ Esteve Terradas 1, Edifici RDIT, Campus PMT-UPC, 08860 Castelldefels, Spain
[14] Institute of Space Sciences, ICE-CSIC, Campus UAB, Carrer de Can Magrans s/n, 08913, Bellaterra, Barcelona, Spain
[15] Instituto de Física, Universidad Nacional Autónoma de México, Circuito de la Investigación Científica, Ciudad Universitaria, Cd. de México C. P. 04510, Mexico
[16] NSF NOIRLab, 950 N. Cherry Avenue, Tucson, AZ 85719, USA
[17] Institució Catalana de Recerca i Estudis Avançats, Passeig de Lluís Companys, 23, 08010 Barcelona, Spain
[18] Institut de Física d'Altes Energies (IFAE), The Barcelona Institute of Science and Technology, Edifici Cn, Campus UAB, 08193, Bellaterra (Barcelona), Spain
[19] Departamento de Física, Universidad de los Andes, Cra. 1 No. 18A-10, Edificio Ip, CP 111711, Bogotá, Colombia
[20] Observatorio Astronómico, Universidad de los Andes, Cra. 1 No. 18A-10, Edificio H, CP 111711 Bogotá, Colombia
[21] University of Virginia, Department of Astronomy, Charlottesville, VA 22904, USA
[22] Fermi National Accelerator Laboratory, PO Box 500, Batavia, IL 60510, USA
[23] Institut d'Astrophysique de Paris. 98 bis boulevard Arago. 75014 Paris, France
[24] IRFU, CEA, Université Paris-Saclay, F-91191 Gif-sur-Yvette, France
[25] Department of Physics, Southern Methodist University, 3215 Daniel Avenue, Dallas, TX 75275, USA
[26] Department of Physics and Astronomy, University of California, Irvine, 92697, USA
[27] The Ohio State University, Columbus, OH 43210, USA
[28] Departament de Física, Serra Húnter, Universitat Autònoma de Barcelona, 08193, Bellaterra (Barcelona), Spain
[29] Department of Physics and Astronomy, Siena University, 515 Loudon Road, Loudonville, NY 12211, USA
[30] Department of Physics and Astronomy, University of Waterloo, 200 University Avenue W, Waterloo, ON N2L 3G1, Canada
[31] Perimeter Institute for Theoretical Physics, 31 Caroline Street North, Waterloo, ON N2L 2Y5, Canada
[32] Waterloo Centre for Astrophysics, University of Waterloo, 200 University Avenue W, Waterloo, ON N2L 3G1, Canada
[33] Instituto de Astrofísica de Andalucía (CSIC), Glorieta de la Astronomía, s/n, E-18008 Granada, Spain
[34] Departament de Física, EEBE, Universitat Politècnica de Catalunya, c/Eduard Maristany 10, 08930 Barcelona, Spain
[35] Department of Physics and Astronomy, Sejong University, 209 Neungdong-ro, Gwangjin-gu, Seoul 05006, Republic of Korea
[36] CIEMAT, Avenida Complutense 40, E-28040 Madrid, Spain
[37] Department of Physics, University of Michigan, 450 Church Street, Ann Arbor, MI 48109, USA
[38] University of Michigan, 500 S. State Street, Ann Arbor, MI 48109, USA
[39] Department of Physics & Astronomy, Ohio University, 139 University Terrace, Athens, OH 45701, USA
[40] National Astronomical Observatories, Chinese Academy of Sciences, A20 Datun Road, Chaoyang District, Beijing 100101, People's Republic of China
Received 2026 February 22; revised 2026 May 5; accepted 2026 May 7; published 2026 June 5

Abstract

Emission-line galaxies (ELGs) are an important tracer of baryon acoustic oscillations (BAOs) and large-scale structure at $z > 1$. In this work, we investigate the feasibility of using deep wide-area multiband imaging (e.g., from the Rubin Observatory) to efficiently select high-redshift ELGs. Using Hyper Suprime-Cam *grizy* photometry and COSMOS2020 many-band photometric redshifts, we design simple color cuts guided by a probabilistic random forest classifier to select galaxies at $z = 1.1$–1.6. We then empirically test and refine these color cuts using two samples of galaxies with deep spectroscopy and broad color coverage obtained with the Dark Energy Spectroscopic Instrument (DESI). Compared to DESI ELGs at $z = 1.1$–1.6, we achieve a higher redshift-measurement success rate (89% versus 69%), a much higher correct redshift-range success rate (84% versus 34%), and a far higher net surface density yield (1372 deg^{-2} versus 660 deg^{-2}). Combining our sample with current DESI ELGs would increase the net ELG number density by a factor of $\sim$2.5, moving it out of the shot-noise limited regime and reducing the uncertainties on the BAO scale parameter at $z = 1.1$–1.6 by a factor of $\sim$2 at the highest redshifts. We also test selections using shallower photometry and obtain qualitatively similar results.

Unified Astronomy Thesaurus concepts: Emission line galaxies (459)

1. Introduction

When the Universe was still very young and hot, before the first atoms could form, baryons and photons were coupled into a single fluid. The radiation pressure associated with this fluid caused sound waves to propagate outward from higher-density regions, commonly known as baryon acoustic oscillations (BAOs). The distance these sound waves could travel before radiation and matter decoupled imprints a characteristic scale upon the clustering of matter, enabling a powerful probe of the expansion history of our Universe and the nature of dark energy using the late-time clustering of galaxies on the sky (e.g., see Section 4 of D. H. Weinberg et al. 2013). Accurately detecting and interpreting the BAO signal typically involves measuring many hundreds of thousands of spectroscopic redshifts and measuring statistics that describe their clustering. The cosmology community has therefore endeavored to design galaxy redshift surveys with sufficient number densities, volume, and reliability of redshift measurements. In this paper, we will investigate new selection methods that take advantage of upcoming imaging datasets and could be used for future spectroscopic surveys.

The first BAO detection by D. J. Eisenstein et al. (2005) was done using data from the Sloan Digital Sky Survey (SDSS; D. G. York et al. 2000; D. J. Eisenstein et al. 2001). That same year, the BAO was also detected using data from the final 2dF Galaxy Redshift Survey (S. Cole et al. 2005). Over the last two decades, there has been significant progress in assembling massive spectroscopic surveys for measuring the BAO feature, some of which include WiggleZ (M. J. Drinkwater et al. 2010), BOSS (K. S. Dawson et al. 2013), and eBOSS (K. S. Dawson et al. 2016). These surveys have been able to place strong constraints on the dark energy equation of state between redshifts $0.1 < z < 1.0$.

To get even tighter cosmological constraints using BAO, galaxy redshift surveys must reach higher redshifts and have increased sky area coverage to probe larger volumes and span a greater fraction of cosmic history. For redshifts up to $z \sim 1$, luminous red galaxies (LRGs) have represented an ideal target class, as they can be readily identified via the 4000 Å break (A. Prakash et al. 2016) and their redshifts can be determined robustly via the strong absorption features in their spectra (R. Zhou et al. 2023a). The primary target class at the highest redshifts (extending to $z \sim 4$) has been quasars, which are rarer but can be selected by ultraviolet or infrared excesses in their continuum out to very high redshift (A. D. Myers et al. 2015; E. Chaussidon et al. 2023). At intermediate redshifts, the primary target class in current surveys is emission-line galaxies (ELGs), the selection of which will be the focus of this paper.

ELGs exhibit very strong emission lines in their spectrum as they are selected at an epoch where the star formation rate (SFR) of the Universe was much higher than it is today (for a recent review, see N. M. F. Schreiber & S. Wuyts 2020). An extremely useful feature that is common in the spectra of these galaxies is the [O II] doublet at 3726, 3729 Å. This doublet provides a reliable method of measuring spectroscopic redshifts (hereafter spec-z or $z_{\rm spec}$) due to its strength and small wavelength separation. Furthermore, ELGs are ubiquitous over $1 < z < 1.6$, making them the ideal tracers for measuring the BAO signal at these redshifts. Past $z \sim 1.6$, the [O II] doublet moves outside the wavelength window of the DESI spectrograph, making objects beyond that redshift less valuable as targets.

The current state-of-the-art survey for BAO cosmology is the Dark Energy Spectroscopic Instrument (DESI; DESI Collaboration et al. 2016, 2022; E. F. Schlafly et al. 2023). Roughly one-third of the targets will be composed of ELGs at redshifts $0.6 < z < 1.6$ (A. Raichoor et al. 2023). DESI recently released BAO distance scale measurements from the first 2 yr of data using galaxy, quasar, and Lyα forest tracers (M. Abdul Karim et al. 2025; A. G. Adame et al. 2025a, 2025b; DESI Collaboration et al. 2025). Combined with either cosmic microwave background (CMB) or type Ia supernova measurements, DESI results prefer a time-varying dark energy equation of state, a direct tension with the current Λ cold dark matter (CDM) paradigm that will need to be confirmed or excluded with future DESI data.

DESI ELG_LOP (DESI ELGs) targets were selected using photometry in the optical g, r, and z using data from the DESI Legacy Imaging Surveys (A. Dey et al. 2019). For ELGs, the resulting selections were affected by both the limited number of optical bands available and the targets having magnitudes near the 5σ depth of that imaging, making the sample selection sensitive to systematics that could affect depth. Consequently, DESI ELGs exhibit significant density fluctuations across the DESI footprint (exceeding 20% in some regions) and provide a relatively low efficiency of selecting objects beyond the redshift range covered by LRGs, providing only around 660 objects deg^{-2} with robust redshift classifications between $1.1 < z < 1.6$ (A. Raichoor et al. 2023). In comparison, the DESI LRG selection (R. Zhou et al. 2023a), which targets objects significantly brighter than the limits of the Legacy Survey photometry, exhibits a much more uniform density of targets across the sky, totaling 476 deg^{-2} objects with reliable redshifts.

The utility of a more efficient selection algorithm for high-z ELGs that can take advantage of new, deeper imaging datasets is highlighted in K. Dawson et al. (2022). In particular, a more efficient ELG selection would improve clustering statistics at high redshifts with new DESI spectroscopy. Better imaging is now available through wide-field surveys like Hyper Suprime-Cam Subaru Strategic Program (HSC; H. Aihara et al. 2017) and will soon be available from the Vera C. Rubin Observatory Legacy Survey of Space and Time (LSST; Ž. Ivezić et al. 2019), providing more depth and additional photometric bands that are invaluable in correctly identifying spectral features to enable target selection of ELGs at high redshift. A cleaner and denser selection of DESI ELGs using HSC or LSST imaging would allow for a DESI-II survey to provide definitive BAO cosmology constraints at redshifts $1.1 < z < 1.6$.

In this paper, we use existing datasets with LSST-like depth to develop a more efficient ELG target selection algorithm and test the feasibility of increasing the current DESI ELG sample by roughly a factor of ∼3 via a future DESI-II survey (D. J. Schlegel et al. 2022). We provide a detailed description of the BAO distance scale improvements that would be obtained from larger samples in Section 2. In Section 3, we discuss the photometric and spectroscopic data used. In Section 4, we optimize and finalize the selection cuts for our spectroscopic sample and compare directly to results from DESI. Finally, we summarize our work and findings in Section 5.

2. Potential Impacts of Enlarging the DESI ELG sample

In this section, we describe the improvements to BAO measurement uncertainties that would result from enlarging the DESI ELG sample at redshifts $1.1 < z < 1.6$. We estimate these improvements using the `FishLSS`[41] code, which has been shown to agree well with the traditional forecasting method of H.-J. Seo & D. J. Eisenstein (2007). More specifically, we take the values within Table 2.3 of A. Aghamousa et al. (2016) as the ELG number density that would result from the full DESI survey and approximate the ELG linear bias as $b(z) = 0.84/D(z)$, where $D(z)$ is the growth factor normalized to unity today.[42] We split the ELG sample into four linearly spaced redshift bins with $\Delta z = 0.2$ covering the range $0.7 < z < 1.5$ and assume a total 14,000 deg^2 sky coverage. We note that using smaller area would result in less gain than what is reported in this work. In each redshift bin, the errors on the BAO distance parameters ($\alpha_\perp$ and $\alpha_\parallel$) are derived from the post-reconstruction power spectrum with the “Rec-Sym” convention using the Zel’dovich approximation (S.-F. Chen et al. 2019). Here, $\alpha_\perp$ and $\alpha_\parallel$ correspond to separations transverse to the line of sight that depend on differences in angle and separations along the line of sight that depend on differences in redshift, respectively. We fix the cosmology to the fiducial values listed in Table 2 of N. Sailer et al. (2021) and marginalize over the linear bias parameter and the coefficients of 15 polynomials of the form $k^n\mu^{2m}$ (for $n = 0, 1, 2, 3, 4$ and $m = 0, 1, 2$) to remove broadband information. The fiducial values of higher-order bias parameters and the scale cuts used when computing the Fisher matrix are all identical to those used in N. Sailer et al. (2021).

The resulting estimates of the improvements on the uncertainties of $\alpha_\perp$ and $\alpha_\parallel$ as a function of the factor by which the ELG number density increases compared to the full DESI survey are shown in Figure 1. The solid black vertical line denotes the expectation for the final DESI ELG sample for comparison. For the three lowest-redshift bins, gains are quite modest for expansions of the sample by >2× . In contrast, for

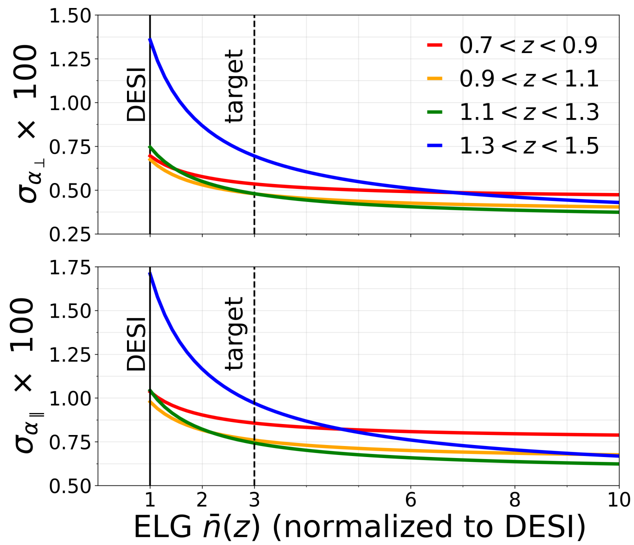

Figure 1. 1σ uncertainty on the BAO scale parameter α as a function of the factor by which the ELG number density is increased compared to the expected final DESI sample (solid black), for measures of both the transverse scale ($\alpha_\perp$) and the line-of-sight scale ($\alpha_\parallel$). Here, the x-axis is relative to the current DESI ELGs, and the y-axis is in terms of percent. The biggest gains are found for the $1.3 < z < 1.5$ redshift bin (blue curve), where expanding the ELG sample at these redshifts by ∼3× (indicated by the dashed black line) would yield a factor of ∼2 improvement on $\alpha_\perp$ and $\alpha_\parallel$. Enlarging the sample by more than this factor would yield only marginal additional improvements.

the highest-redshift bin ($1.3 < z < 1.5$, shown in blue), gains only become slow when the sample is expanded by >3×, a limit marked by the black dashed vertical line. Increasing the number density by more than this would result in only marginal decreases in the error on either parameter. Given this, we want to obtain a sample with a surface density yield of 1370 deg^{-2}, compared to 660 deg^{-2} for the current DESI sample. These calculations are made based on the original 5 yr DESI survey design. The change in area from 14,000 deg^2 to 17,000 deg^2 expected from the extended DESI program would lower each curve by a constant factor. It is also important to note that these gains are after fiber assignment, not before.

3. Data

Based on the estimates in Section 2, we aim to augment the current DESI ELG sample at $z > 1.1$ by a factor of ∼3 by combining the current sample with the one we optimize in this work. In this section, we describe the photometric and spectroscopic data used to design new ELG selections that accomplish this goal. We use wide imaging data from the third data release of HSC containing LSST-like *grizy* photometry. We use LSST-like deep *ugrizy* photometry from the COSMOS2020 catalog and the many-band LePHARE photo-z’s. We use the DESI spectroscopic truth sample for our final selection optimization, which was designed for studying the imaging systematics of the ELG sample.

3.1. HSC

In this work, we use the wide imaging from the third data release (DR3) of HSC (H. Aihara et al. 2022). This catalog includes *grizy* photometry with point-spread function (PSF) depths of 26.5/26.5/26.2/25.2/24.4, respectively. HSC wide is slightly deeper than LSST Y2 in some bands, but we demonstrate that this does not qualitatively affect the metrics

[41] https://github.com/NoahSailer/FishLSS

[42] We hold the linear bias fixed to its fiducial value when rescaling the ELG number density, but note that the linear bias should decrease modestly if lower-luminosity but still star-forming objects are included (A. L. Coil et al. 2008).

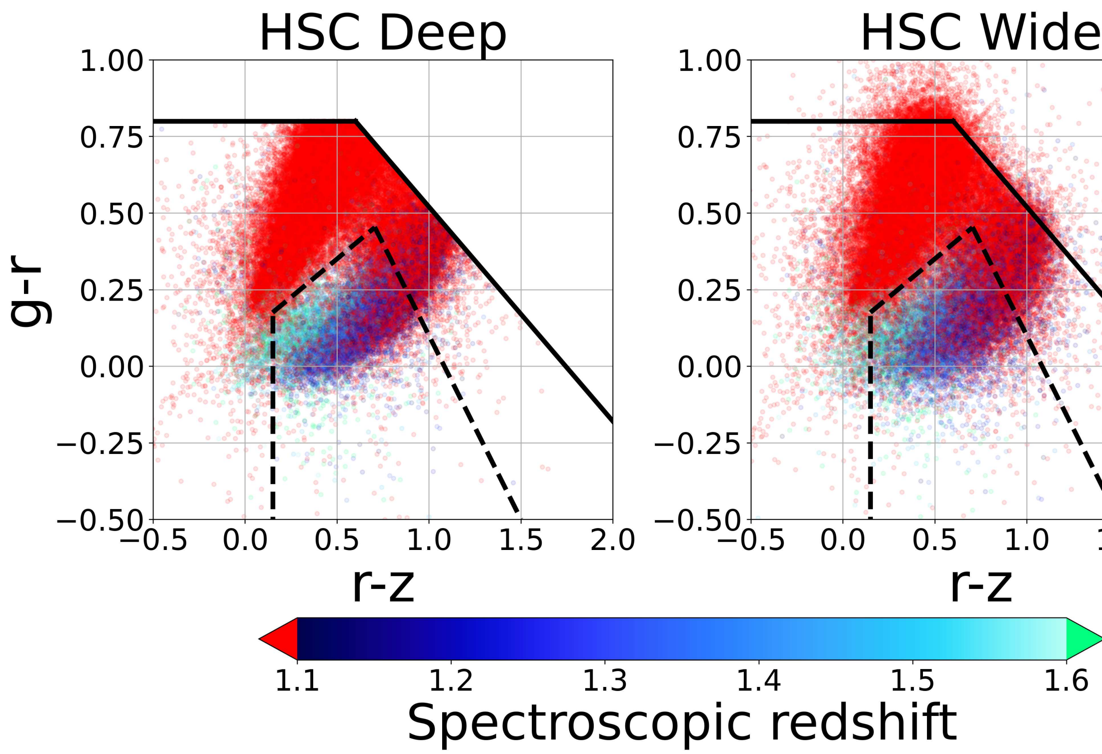

Figure 2. Color–color diagrams of the DESI spec-truth sample using $g-r/r-z$ plotted using imaging from either deep (left) or wide (right) depth HSC imaging, with galaxies color-coded according to their spec-z. This sample was obtained using HSC deep photometry. We show the color cuts for the standard DESI ELG sample (dashed black lines) and the spec-truth sample (solid black). Although the wide photometry is noisier, the selection limits are far enough from where ELGs reside in color space to ensure that the sample still retains all ELG-like objects down to the desired depths.

of interest for selecting high-z ELGs in Appendix B. The HSC bands are around 2 mag deeper than the depths of the Legacy Survey imaging that was used for DESI ELG targets and have the addition of i/y. The deeper and additional bands are important for greatly improving the efficiency of ELG target selections. We used the Schlegel, Finkbeiner, and Davis extinction map for Milky Way extinction corrections (D. J. Schlegel et al. 1998).

3.2. COSMOS2020

One avenue we use for testing the viability of selecting a large sample of ELGs at $1.1 < z < 1.6$ using LSST-like photometry is the Farmer version of the COSMOS2020 catalog (J. R. Weaver et al. 2022). This catalog includes deep Canada–France–Hawaii Telescope (CFHT) Megacam u (M. Sawicki et al. 2019) and HSC *grizy* (H. Aihara et al. 2019) photometry reaching depths of 27.7/28.1/27.8/27.6/27.2/26.5 in a $2''$ aperture for each band, respectively. The corresponding PSF depths for the HSC imaging are 28.3/28.1/28.0/27.5/26.6, respectively.

In total, this catalog contains photometry from more than 30 passbands, reduced with matched-model algorithms using the `Tractor` software (D. Lang et al. 2016). It also includes photometric redshifts (photo-z's) that have been derived using all of the available passbands using both the LePHARE (S. Arnouts & O. Ilbert 2011) and EAZY (G. B. Brammer et al. 2008) spectral energy distribution template fitting algorithms. While both algorithms typically provide similar redshift estimates, we adopt the LePHARE photo-z's for our analysis because EAZY results exhibited anomalies at $z > 1.5$. In particular, EAZY produced unrealistically high photo-z's out to $z \sim 12$. Although the many-band LePHARE photo-z's are much more reliable than photo-z's based only on broad-band optical photometry, they still exhibit larger uncertainties than spectroscopic redshifts and are only available within small areas (making cosmic variance more of an issue); in Appendix C, we present tests of these redshifts for ELG-like samples with DESI spec-z measurements.

3.3. Spectroscopic Data

In addition to the COSMOS2020 sample, we also make use of a spectroscopic sample that was originally designed for studying the imaging systematics of the DESI ELG sample (R. Zhou et al. 2026, in preparation). This sample was targeted using deep DECam (B. Flaugher et al. 2015) and HSC imaging with selection cuts that extend well beyond those used to select DESI ELGs to capture all of the objects that could scatter into the DESI sample due to photometric uncertainties. From here on, we refer to this sample as the "spec-truth" sample. Figure 2 shows the spec-truth (solid black lines) and DESI ELG (dashed black lines) color cuts in $g-r$ versus $r-z$ color space. The spec-truth sample was selected using HSC deep photometry from DR3 (left panel), but the broad color cuts of this sample should include all of the ELGs at $z = 1.1$–1.6, even when selecting objects using the shallower HSC wide photometry.

The selection cuts for the spec-truth sample using DECam photometry were

$$19.5 < g_{\rm fiber} < 24.5, \quad (1a)$$

$$g - r < 0.9, \quad (1b)$$

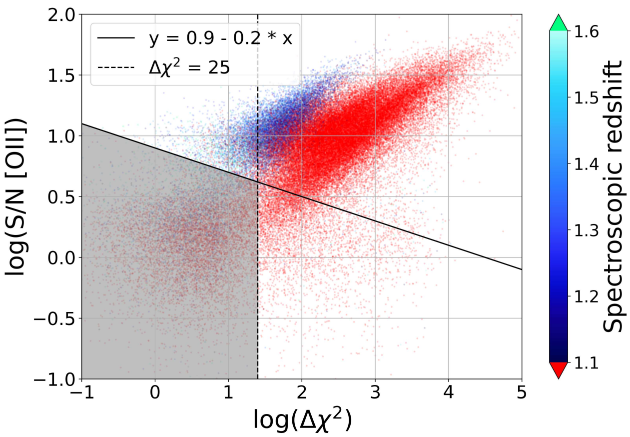

Figure 3. [O II] flux S/N vs. the $\Delta\chi^2$ between the best-fit and second best-fit redshift solutions for the spec-truth sample (points color-coded by spec-z). We consider objects above the solid black diagonal line (the DESI ELG reliable-redshift criteria; A. Raichoor et al. 2023) or rightward of the dashed black line ($\Delta\chi^2$) to have reliable redshifts (i.e., not in the shaded region of this diagram).

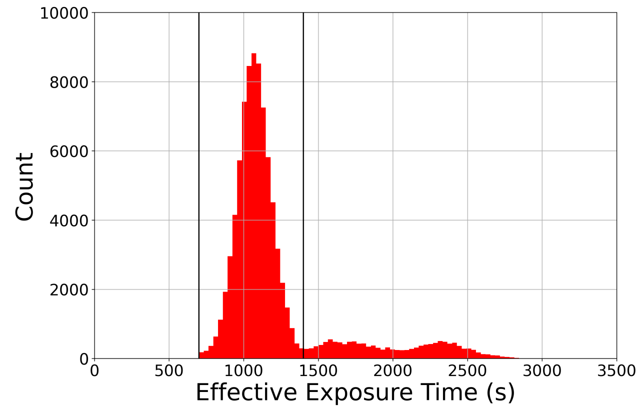

Figure 4. The effective exposure time distribution for the spec-truth sample. Only those objects whose exposure times are within the range bounded by the solid black vertical lines ($700 < t < 1400$ s) are used for calculating redshift-measurement success rates, whereas all objects with $t > 700$ s are included when calculating the fraction of targets in the desired redshift range ($1.1 < z < 1.6$). The metrics used are described in more detail in Section 4.

and

$$g - r < 1.32 - 0.7 \times (r - z), \quad (1c)$$

where $g_{\rm fiber}$ is the g-band fiber magnitude (i.e., the magnitude corresponding to the expected flux within a DESI fiber aperture). The spec-truth selection cuts applied based on HSC photometry were

$$19.5 < g_{\rm aperture} < 24.55, \quad (2a)$$

$$g - r < 0.8, \quad (2b)$$

and

$$g - r < 1.22 - 0.7 \times (r - z), \quad (2c)$$

where $g_{\rm aperture}$ is the g-band magnitude within a $1\farcs5$ aperture. Objects were included in the observed sample if they met either the HSC or DECam selection criteria.

This sample was observed using the DESI instrument in the COSMOS field on 2024 March 9–13, utilizing 25 overlapping tiles on the sky with 1000 s of effective exposure time for each tile (DESI Collaboration et al. 2016, 2022; T. N. Miller et al. 2024; C. Poppett et al. 2024). We use the standard DESI definition of effective exposure time (see Equation (22) in J. Guy et al. 2023). In total, spectra for 95,443 unique objects were obtained. After applying a minimum effective exposure time cut of $t > 700$ s and cross-matching with the HSC wide catalog, the total number of ELG-like objects available for our analysis was 87,512.

In Figure 3, we plot the [O II] flux signal-to-noise ratio (S/N) versus the $\Delta\chi^2$ between the best-fit and second best-fit redshift solutions for the spectroscopic truth sample (where points are colored by their spec-z). To select objects with reliable spec-z's, we apply similar cuts to those used for selecting DESI ELGs (A. Raichoor et al. 2023) based on the S/N of the flux of the [O II] $\lambda\lambda$ 3726, 3729 Å emission-line doublet and the $\Delta\chi^2$ between the best-fit and second best-fit spectral template. These cuts were developed based on visually inspecting redshift fits to galaxy spectra. After determining that galaxies with $\Delta\chi^2 > 25$ below the solid black line should contain significant redshift information in their spectrum, we add this to our reliable-redshift cuts. The final reliable-redshift cuts used for this work are

$$\log(\text{flux [OII]}) > 0.9 - 0.2 \times \log(\Delta\chi^2) \textbf{ OR } \Delta\chi^2 > 25, \quad (3)$$

where the first term is the reliable-redshift cut used for DESI ELGs. We find that 68,035 of these galaxies have reliable spec-z measurements after applying the $\Delta\chi^2$ and [O II] S/N criteria cuts. These criteria constitute a more inclusive version of what was used in A. Raichoor et al. (2023) for the final DESI ELG sample.[43]

Figure 4 shows the effective exposure time distribution for the spec-truth sample. In order to make as fair a comparison as possible to the DESI ELG sample, we only use objects with effective exposure times in the range $700 < t < 1400$ s (region between black solid vertical lines) for calculating redshift-measurement success rate (i.e., how often a targeted object yielded a secure redshift measurement). However, we use all objects with effective exposure times above 700 s to calculate the fraction of objects at $1.1 < z < 1.6$.

4. Design of Selection Criteria

In this section we describe our method of acquiring initial color cuts and optimizing these cuts to cleanly select high-redshift ELGs between $1.1 < z < 1.6$. In particular, we wanted to obtain a sample of ELGs with very high redshift-measurement and redshift-range success rates, in addition to our goal of a sample with a surface density yield of 1370 deg^{-2}. We then compare our optimized sample to the current DESI ELGs over $1.1 < z < 1.6$.

4.1. Initial Design of Color Cuts Using a Random Forest

We use a random forest (RF; L. Breiman 2001) to classify whether COSMOS2020 galaxies are high-z ELGs based on their *ugrizy* photometry. RF classifiers deliver performance comparable to more sophisticated machine learning algorithms with minimal hyperparameter tuning and robustly handles degenerate information, making them well suited for our needs

[43] If we instead only use the reliable-redshift criteria employed for DESI ELGs, we see a reduction of the redshift-measurement success rate from 89% to 87% and redshift-range success rate from 84% to 83% for our final optimized selection.

of developing a good initial set of color cuts. We train the RF using the deep LSST-like COSMOS2020 *ugrizy* magnitudes and all color combinations to predict which galaxies are within the range $z = 1.1$–1.6 based on the many-band LePHARE photo-z's.

The RF proved to be very successful at selecting high-z ELGs. Using a receiver operating characteristic (ROC; T. Fawcett 2006) curve, a common tool for evaluating classifiers, the RF achieved an impressive area-under-the-ROC-curve of 0.960 (compared to 1 for a perfect classifier). This level of performance corresponds to a sample that is both highly pure and complete.

We then use the RF classifier probabilities (of being a high-z ELG) to design a set of color cuts to simplify the selection, ease simulation efforts, and maximize interpretability. First, we determine which colors are most influential on the RF classifier by determining the permutation feature importance for all input properties (G. König et al. 2020). We find that the combination of $r - i$ and $i - y$ colors are enough to capture most of the useful information. The next most important feature is $i - z$, which we consider for our final optimized sample (see Section 4.2). These colors are not unique, as other color combinations exist that would contain degenerate information, which would lead to similarly effective selections. The color cuts are

1. $i - y - 0.19 + \text{offset}_1 > r - i$,
2. $i - y > 0.35 + \text{offset}_2$,

where offset_1 and offset_2 are both zero (but are optimized in Section 4.2 below with the help of spectroscopy).

4.2. Optimizing Color Cuts

After developing initial color cuts based upon COSMOS2020, we use the spec-truth sample to explore modifications to those cuts that would maximize the fraction of objects with secure redshifts in the desired redshift range while yielding a net surface density yield close to our goal of 1370 deg^{-2}, corresponding to our target of increasing the density of high-z ELGs by $\sim 3\times$ (see Section 2). In addition, we want the final sample to have a limiting magnitude not much fainter than the DESI ELG selection. We test both g-fiber and r-fiber selections and find limiting with the g-fiber to be better for selecting high-z ELGs. This is not too surprising, as the g-band is closer to the rest UV and so is a better tracer of SFR and, hence, [O II] flux. To characterize and optimize the resulting samples, we consider several metrics: redshift-measurement success rate, redshift-range success rate, target density, and net surface density yield.

First, we define the redshift-measurement success rate,

$$f_{\text{reliable}} = \frac{N_{\text{reliable}}^{700 < t < 1400}}{N_{\text{total}}^{700 < t < 1400}}, \quad (4)$$

where $N_{\text{total}}^{700 < t < 1400}$ is the number of objects with integration time between $t = 700$ and 1400 s that pass our optimized color cuts and g-fiber limiting magnitude, and $N_{\text{reliable}}^{700 < t < 1400}$ are the subset of those objects that also pass the reliable z_{spec} cuts. The exposure time cuts are applied both (1) to exclude objects with bad exposures or negligible effective observation time and (2) to exclude objects with exposures significantly longer than a typical DESI ELG exposure (A. Raichoor et al. 2023) to ensure that redshift-measurement success rates can be compared fairly between samples.

To compute the redshift-range success rate, we must first compute the fraction of all objects (with $t > 700$ s) with $z_{\text{spec}} = 1.1$–1.6,

$$f_{z = 1.1 - 1.6}^{t > 700} = \frac{N_{z = 1.1 - 1.6}^{t > 700}}{N_{\text{total}}^{t > 700}}, \quad (5)$$

where $N_{\text{total}}^{t > 700}$ is the total number of objects with an integration time of $t > 700$ s that pass our optimized color cuts and g-fiber limiting magnitude and have reliable z_{spec}, and $N_{z = 1.1 - 1.6}^{t > 700}$ is the subset that are within $1.1 < z < 1.6$. In this case, we include information from objects with exposure times longer than those typically used for DESI ELGs to maximize the sample size; since we are not assessing the redshift-measurement success rate in this factor, a maximum exposure time cut is not needed.

Now we can calculate the redshift-range success rate (i.e., the fraction of targets with typical DESI ELG exposure times that are in the desired redshift range with successfully measured z_{spec})

$$f_{z = 1.1 - 1.6}^{700 < t < 1400} = f_{\text{reliable}} \times f_{z = 1.1 - 1.6}^{t > 700}, \quad (6)$$

where f_{reliable} accounts for redshift-measurement success rate for $700 < t < 1400$ s exposures only.

We calculate the target density,

$$\Sigma_{\text{target}} = \frac{N_{\text{selected}}}{A}, \quad (7)$$

where N_{selected} is the number of galaxies passing a given set of cuts within the HSC wide catalog used, and A is the sky area of the HSC field ($\sim 16\ \text{deg}^2$, ignoring masked-out regions that likely reduce the effective area by a few percent). Finally, we define our net surface density yield to be

$$\Sigma_{\text{yield}}^{z = 1.1 - 1.6} = \Sigma_{\text{target}} \times f_{z = 1.1 - 1.6}^{700 < t < 1400}. \quad (8)$$

We use a minimization method to optimize a set of free parameters defining our final selection cuts. The four parameters include the two color cut offsets for the color cuts obtained using the RF classifier, an $i - z$ cut (the next most important feature in the RF feature permutation), and a g-fiber limiting magnitude applied to the sample. As described in Section 2, the largest gains in enlarging the DESI ELG sample would be at high-z (where increasing past 1370 deg^{-2} would only result in marginal improvement to BAO measurements). Given this, we optimize our sample to maximize the redshift-range success rate of high-z ELGs and obtain a net surface density yield close to 1370 deg^{-2}. We employ the `scipy.optimize.minimize` routine (P. Virtanen et al. 2020) for this purpose. Specifically, we minimize a loss function L defined by:

$$L = -f_{z = 1.1 - 1.6}^{700 < t < 1400} \times 100 + w \times (\Sigma_{\text{yield}}^{z = 1.1 - 1.6} - 1370\ \text{deg}^{-2})^2, \quad (9)$$

where w is a weight value within the range from 0.003–0.0012. After providing initial guesses for the optimal values of the four free parameters, we were able to extract values that maximize redshift-range success rate with a net surface density

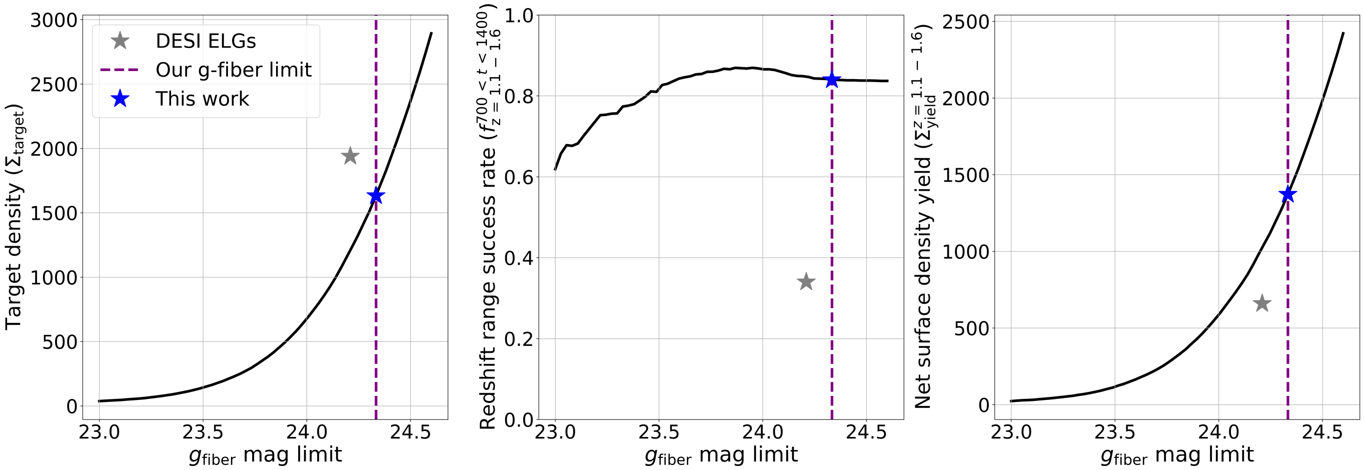

Figure 5. Target density ($\Sigma_{\rm target}$), redshift-range success rate ($f^{700\,<\,t\,<\,1400}_{z\,=\,1.1\,-\,1.6}$), and the net surface density yield ($\Sigma^{z\,=\,1.1\,-\,1.6}_{\rm yield}$) for different g-fiber limiting magnitudes (black solid lines). The g-fiber limiting magnitude optimized to yield a net surface density of 1372 redshifts per square degree is indicated by the dashed purple lines in each panel. The DESI ELG sample is shown by the gray stars, while the results of our sample are shown by the blue stars. Despite both samples having similar target densities and g-fiber limiting magnitudes, the HSC-based selection we present here is much more efficient at yielding redshifts in the desired range, as can be seen by the much higher values of redshift-range success rate (middle panel) and net surface density yield (right panel) obtained for it.

Table 1
Comparison of Metrics for Our ELG Selection to Those for DESI ELGs

	$f_{\rm reliable}$	$f^{700<t<1400}_{z=1.1-1.6}$	$\Sigma_{\rm target}$ (deg^{-2})	$\Sigma^{z\,=\,1.1\,-\,1.6}_{\rm yield}$ (deg^{-2})
DESI ELGs	69%	34%	1940	660
This work	89%	84%	1632	1372

Note. By selecting ELGs with deeper photometry in redder bands, we can achieve more than a factor of 2 higher fraction of targets with reliable-redshift measurements in the desired redshift range ($f^{700\,<\,t\,<\,1400}_{z\,=\,1.1\,-\,1.6}$). Because of this, we are able to more than double the net surface density yield ($\Sigma^{z\,=\,1.1\,-\,1.6}_{\rm yield}$) while targeting fewer total targets per square degree than the DESI ELG sample.

yield close to our goal of 1370 deg^{-2}. The final cuts we obtain for our optimized sample are:

1. $g_{\rm fiber} < 24.33$,
2. $i - y - 0.16 > r - i$,
3. $i - y > 0.43$, and
4. $i - z > 0.45$.

The i and z bands are instrumental in selecting high-z ELGs because they span the wavelengths where the 4000 Å break moves between at $z \sim 1.1$.

This work started before the conception of the spec-truth sample, so our initial efforts involved developing target selection cuts for a similar sample using LSST-like *ugrizy* photometry and many-band photo-z's from COSMOS2020. We used these cuts to obtain DESI spectroscopy to test these selection criteria, which we refer to as the DESI-II pilot sample (see Appendix A). However, the spec-truth sample superseded the DESI-II pilot sample due to its larger size and broader color cuts, so we use it for all of the results within the main body of this paper.

4.3. Comparison to DESI

The ELG sample that we present here is optimized to cover the redshift range $1.1 < z < 1.6$ in order to allow for direct comparisons to the statistics for the DESI ELG sample in this z range that are presented in Table 4 of A. Raichoor et al. (2023). In Figure 5, we plot the target surface density ($\Sigma_{\rm target}$), the redshift-range success rate ($f^{700\,<\,t\,<\,1400}_{z\,=\,1.1\,-\,1.6}$), and the net surface density yield ($\Sigma^{z\,=\,1.1\,-\,1.6}_{\rm yield}$) resulting from our color cuts as a function of the g-fiber limiting magnitude. The g-fiber magnitude limit we adopt as standard is indicated by the vertical purple dashed line; our sample can be compared directly to the statistics for DESI ELGs from A. Raichoor et al. (2023) that are indicated by red stars. Despite having a similar target density and only going slightly fainter than the DESI ELG sample, our color cuts provide a much denser sample of objects with redshifts in the desired range. We compare our results to DESI ELGs quantitatively in Table 1, using the metrics defined in Section 4.2. We find that the largest improvements are obtained for redshift-range success rate and net surface density yield; our sample outperforms the DESI ELG sample by factors of ~2.4 and ~2.1 in these metrics, respectively.

Figure 6 illustrates the effectiveness of our optimized $r - i/i - y/i - z$ color cuts for selecting ELGs within the redshift range $1.1 < z < 1.6$. Our cuts reject the majority of the low-redshift contamination at $z < 1.1$ (red), while still retaining the galaxies we wish to include, i.e., those that are at $1.1 < z < 1.6$ and yield secure redshifts in ~1000 s exposure times (blue points). Figure 7 shows the completeness of our optimized ELG selection as a function of $z_{\rm spec}$. We define completeness as the fraction of the spec-truth sample at a given redshift (after applying our fiducial g-fiber magnitude cut) that pass our optimized color cuts. Our cuts effectively target the desired high-redshift objects while avoiding the majority of interlopers.

Similarly, we define the interloper rate as the fraction of the spec-truth sample that passes our optimized g-fiber and color

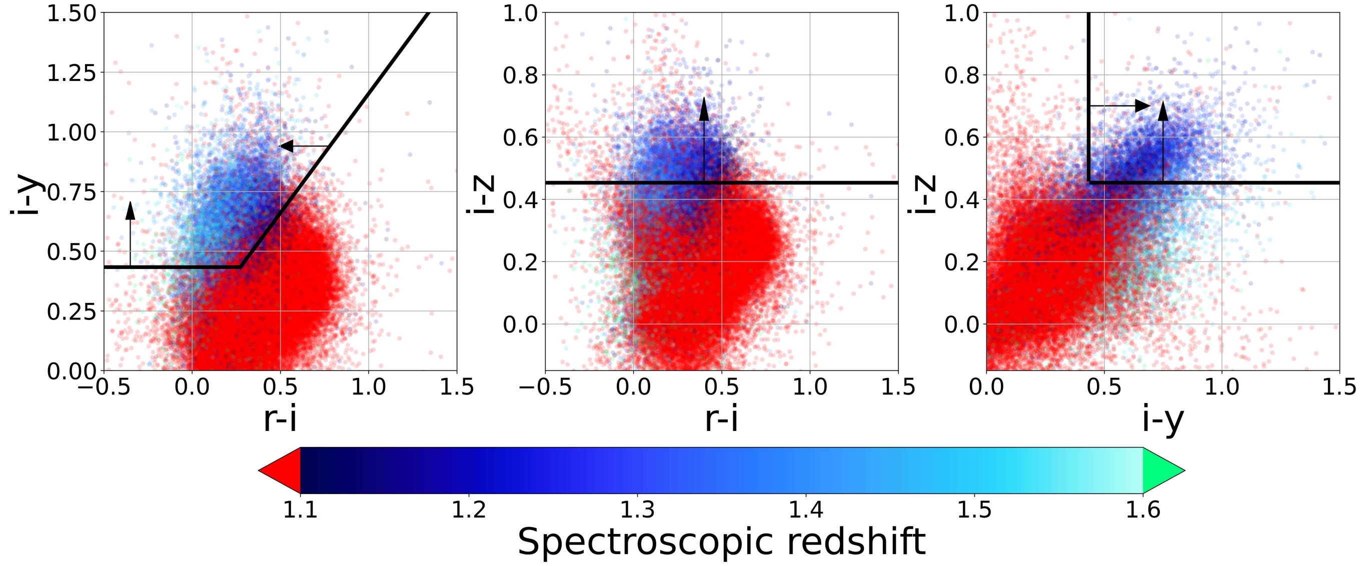

Figure 6. Color–color diagrams of ELGs from the spec-truth sample with reliable z_{spec} measurements, where points are color-coded according to their spectroscopic redshifts. Solid black lines show our final selection cuts, with black arrows indicating on which side of the dividing lines our final sample lies. These cuts are effective at throwing out objects at low redshift (the $z < 1.1$ objects indicated by red points) while maintaining a high completeness for selecting $1.1 < z < 1.6$ galaxies.

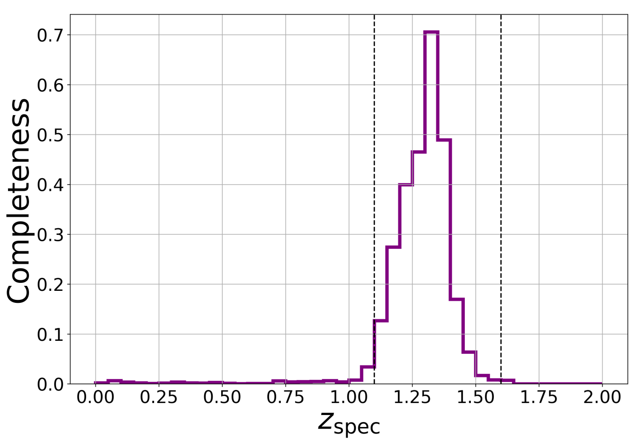

Figure 7. Completeness as a function of z_{spec}. Here, we define completeness as the fraction of the spec-truth sample at a given redshift (after applying our fiducial g-fiber magnitude cut) that passes our optimized color cuts. Our selection cuts target a significant amount of the $1.1 < z < 1.6$ ELG population while avoiding interlopers.

cuts but has a redshift outside of the desired $1.1 < z < 1.6$ range. For $z < 1.1$ interlopers, we calculate this rate based upon galaxies with reliable z_{spec}, obtaining a value of 5%. For $z > 1.6$ interlopers (i.e., ones in a regime where the [O II] doublet cannot be picked up by the DESI spectrograph), we instead use COSMOS2020 LePHARE photo-z's to determine what fraction of selected objects that lack a reliable z_{spec} are in this range. This yields a high-z interloper rate of roughly 14%.

By using COSMOS2020 LePHARE photo-z's, we can also explore how galaxies that did not pass our reliable-redshift criteria populate this color space. Color–color plots for this sample color-coded according to their LePHARE photo-z's are shown in Figure 8. Although these photo-z's are not as reliable as spectroscopic redshift measurements, they still can provide useful information on the nature of the redshift failures. As can be seen in this plot, in addition to excluding low-z objects that are spectroscopically confirmed to be at $z < 1.1$, our optimized cuts also are very effective at rejecting objects that failed to yield secure redshift measurements but are in fact estimated to lie either at $z < 1.1$ or at $z > 1.6$ (the regime where [O II] falls outside of DESI's spectral window so that redshift failures would be expected).

In Figure 9, we compare the distribution of spectroscopic measurements for our optimized sample and a similar sample using slightly shallower LSST/Y2-like photometry (described in Appendix B) directly to DESI ELGs. Both optimized samples suffer from less low-z ($z < 1.1$) contamination while also having a much larger net surface density yield of ELGs within the desired redshift range.

We apply the same methods to optimize selections for a slightly broader redshift range, $1.05 < z < 1.65$, and obtain qualitatively similar results; i.e., our methods can be optimized for somewhat different redshift ranges if desired. Most notably, when optimizing for this broader span, we obtain a slightly higher redshift-range success rate ($f^{700 < t < 1400}_{z = 1.05 - 1.65}$) of 85% as compared to 84% for the $1.1 < z < 1.6$ sample.

A separate question to consider is what fraction of the objects we target would not be part of the existing DESI ELG sample. We find roughly 17% of the spec-truth objects passing our optimized cuts were also DESI LOP targets. To get a more accurate estimate of the net increase of DESI ELGs at $1.1 < z < 1.6$ when combining previously observed objects with our samples, we consider two scenarios: (A) where the same fraction of targets is assigned to fibers as DESI ELGs (69%), and (B) where 100% of our sample is targeted. In scenario (A), we would obtain spectra of 786 deg^{-2} additional ELGs compared to the current sample, for a total increase of $\sim$2.2× in the number of objects at $1.1 < z < 1.6$. In scenario (B), we instead would obtain 1211 deg^{-2} additional ELG spectra, for a total increase of $\sim$2.8×. Averaging these two scenarios gives an increase of the high-redshift ELG density of $\sim$2.5×.

Utilizing the deeper imaging and additional bands from COSMOS2020, we designed and optimized a high-z ELG sample that is denser and more efficient than current DESI

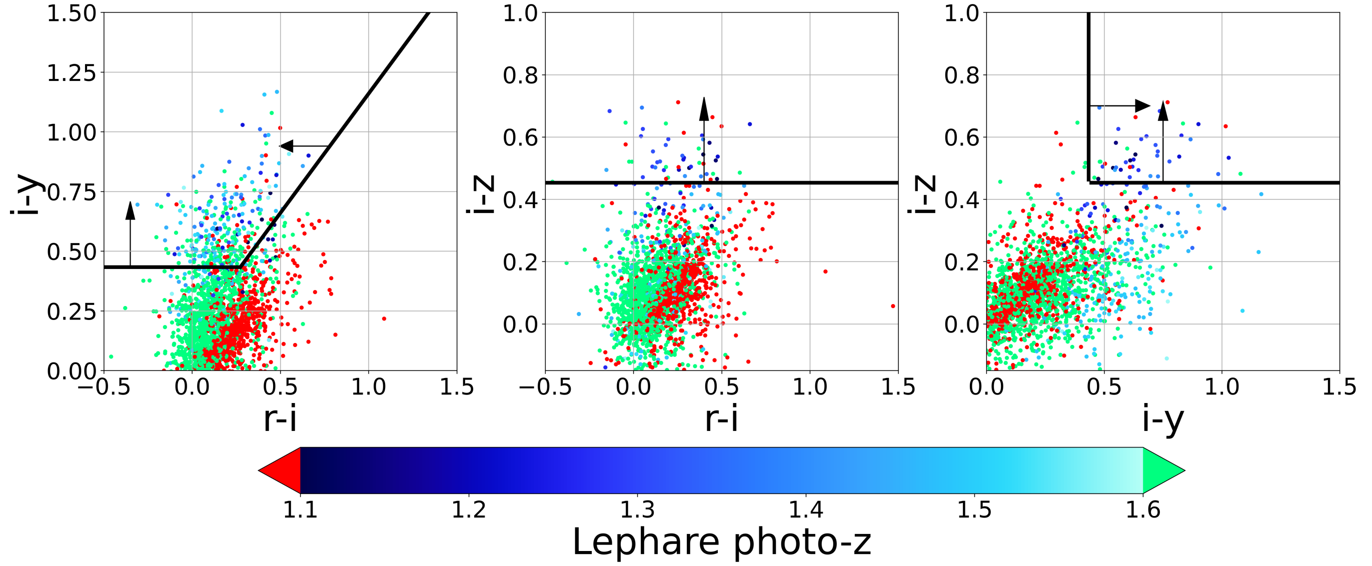

Figure 8. Color–color plot diagrams for galaxies from the spec-truth sample that did not meet the reliable-redshift cuts illustrated in Figure 3, with points color-coded based upon their COSMOS2020 LePHARE many-band photo-z. Solid black lines and arrows show our optimized color cuts. Our results indicate that the color cuts are not only extremely effective at throwing out redshift failures that intrinsically lie below $z < 1.1$ (red) but also are effective in rejecting objects at $z > 1.6$, where the DESI spectrograph would be ineffective in measuring redshifts (green).

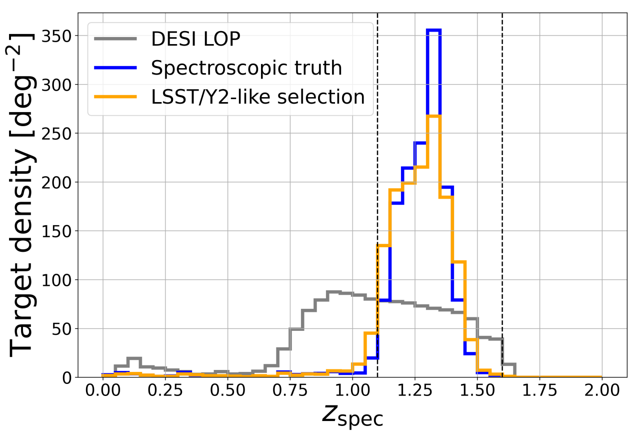

Figure 9. Comparison of the target density of objects as a function of redshift for the DESI ELG sample (gray) compared to the ELGs selected by the optimized cuts presented in Section 4.2 (blue) and a similar selection using artificially degraded photometry (orange). Vertical lines indicate the redshift range $1.1 < z < 1.6$ that our sample is optimized to target. Our cuts do a much better job at excluding low-redshift ($z < 1.1$) objects and consequently produce a much denser sample with galaxies in the desired redshift range for both samples. Rejecting low-z contamination around $z \sim 0.35$ came at the cost of some high-z ELGs near $z \sim 1.5$ (due to the two populations having similar colors).

ELGs. In particular, our sample has a significantly higher redshift-range success rate and net surface density yield; these quantities are improved by factors of $\sim$2.4 and $\sim$2.1, respectively. Combining the current DESI ELG sample with ours would enable significant reductions of BAO errors at $1.1 < z < 1.6$. (as demonstrated in Section 2).

5. Summary and Prospects

In this work, we have demonstrated that current and planned deep multiband imaging datasets can enable the design of efficient high-z ELG selections for future spectroscopic surveys such as a future DESI-II survey. As described in Section 2, by enlarging the current DESI ELG sample close to a factor of 3, we can reduce uncertainties of BAO distance parameters ($\alpha_\perp$ and $\alpha_\parallel$) for high-z ELGs by a factor of 2.

With this goal in mind, we explored different selection criteria for ELGs at $1.1 < z < 1.6$ using *grizy* HSC wide photometry, an RF trained on COSMOS2020 *ugrizy* photometry and LePHARE photo-z's, and results of a dedicated spectroscopic campaign with DESI. Using a simple minimization approach, we obtained a sample optimized for selecting high-redshift ELGs that incorporates cuts in $r - i$, $i - z$, and $i - y$ colors as well as a limit in g-band fiber magnitude. Compared to DESI, the sample has a similar target density ($\Sigma_{\rm target}$) and g-band fiber magnitude limit, yet results in a much denser and efficient ELG selection. The largest improvements are made on redshift-range success rate ($f_{z=1.1-1.6}^{700<t<1400}$) and net surface density yield ($\Sigma_{\rm yield}^{z=1.1-1.6}$), which our sample outperforms by over factors of $\sim$2.4 and $\sim$2.1, respectively.

Combining the current ELG sample with ours would help reduce BAO errors at $z > 1.3$ by around a factor of $\sim$2 (based on the calculations in Section 2). We have also used the DESI spec-truth sample of ELG-like objects to test the performance of photo-z algorithms at predicting their redshifts, finding significant scatter and outliers compared to their spec-z (especially when comparing HSC photo-z's), reinforcing the need for combining photometric information with spectra when designing high-z ELG samples (see Appendix C).

Looking toward the future, it would be interesting to test the feasibility of obtaining an ELG sample like the one described in this work during gray or bright time, rather than the comparatively dark time that was used for the spec-truth observations. Moonlight mostly affects the night-sky continuum spectrum, particularly at the blue end where scattering is greatest. As a result, it should have comparatively little effect on redshift success for our sample, as at $z > 1.1$ the [O II] line will be at >7800 Å , where night-sky emission lines are the dominant background. Obtaining such a sample during gray or bright time could increase the efficiency of a DESI-II program, as its main cosmological samples will focus on $z > 2$

galaxies, for which the primary features of interest are at the blue end of the spectrum, and dark time is necessary.

Another application of the sample selection described here (or a similar selection) would be to produce a purely photometric sample with a well-defined selection and redshift distribution that could be used for CMB cross-correlation analyses. Such samples would build on the photometric LRG selections presented by R. Zhou et al. (2023b), which enable such analyses at lower redshifts. For measurements of lensing cross-correlations, precision redshift measurements for individual objects are not necessary, so long as z-distributions are tight and well understood. Defining such photometric samples would enable constraints on the growth of structure at higher redshifts than LRGs probe, extending the work of N. Sailer et al. (2025) past $z \sim 1$.

Acknowledgments

The efforts of Y.S.H. and J.A.N. were supported by grant DE-SC0007914 from the U.S. Department of Energy Office of Science, Office of High Energy Physics.

This material is based upon work supported by the U.S. Department of Energy (DOE), Office of Science, Office of High-Energy Physics, under contract No. DE–AC02–05CH11231, and by the National Energy Research Scientific Computing Center, a DOE Office of Science User Facility under the same contract. Additional support for DESI was provided by the U.S. National Science Foundation (NSF), Division of Astronomical Sciences under contract No. AST-0950945 to the NSF's National Optical-Infrared Astronomy Research Laboratory; the Science and Technology Facilities Council of the United Kingdom; the Gordon and Betty Moore Foundation; the Heising-Simons Foundation; the French Alternative Energies and Atomic Energy Commission (CEA); the National Council of Humanities, Science and Technology of Mexico (CONAHCYT); the Ministry of Science, Innovation and Universities of Spain (MICIU/AEI/10.13039/501100011033), and by the DESI Member Institutions: https://www.desi.lbl.gov/collaborating-institutions. Any opinions, findings, and conclusions or recommendations expressed in this material are those of the author(s) and do not necessarily reflect the views of the U. S. National Science Foundation, the U. S. Department of Energy, or any of the listed funding agencies.

The authors are honored to be permitted to conduct scientific research on I'oligam Du'ag (Kitt Peak), a mountain with particular significance to the Tohono O'odham Nation.

Y.S.H. thanks the LSST-DA Data Science Fellowship Program, which is funded by LSST-DA, the Brinson Foundation, the WoodNext Foundation, and the Research Corporation for Science Advancement Foundation; his participation in the program has benefited this work.

The authors thank the anonymous referee for providing helpful suggestions.

Software: Astropy (Astropy Collaboration et al. 2013, 2018; Astropy Collaboration et al. 2022), Colorcet (P. Kovesi 2015), Matplotlib (J. D. Hunter 2007), NumPy (C. R. Harris et al. 2020), SciPy (P. Virtanen et al. 2020), SciKit-Learn (F. Pedregosa et al. 2011), Pandas (The pandas development team 2020).

Data Availability

The data used to make the plots in this paper can be found at DOI: 10.5281/zenodo.19835307.

Appendix A
DESI-II Pilot Sample

Prior to the availability of the DESI spec-truth sample, we used the DESI instrument to obtain spectroscopy of a sample of objects intended to investigate the feasibility of using deep wide-area multiband imaging (e.g., from LSST) to efficiently select high-redshift ELGs; we will refer to this as the "pilot sample" in the remainder of this appendix. Analyses of this sample led to similar conclusions to the results based upon the spec-truth sample reported in the main body of this paper. Given its broader targeting color cuts and larger sample size (with over a 3× increase in the number of high-z ELGs), we have used the spec-truth sample for the main analysis of this paper; however, we briefly describe the pilot sample here to document its selection and its implications for high-z ELG selection. This sample should be included in future public DESI data releases.

A.1. Pilot Sample Design

Using HSC wide photometry, COSMOS2020 photometric redshifts, and the aid of an RF classifier to guide the choice of colors to use (following the procedures that are described in detail in Section 4.1), we develop a set of simple $r - i/i - y$ color cuts that can be used to target galaxies likely to be high-redshift ELGs. The resulting cuts are illustrated in Figure 10. Galaxies in the color–color plots in each panel are color-coded according to the fraction that pass an RF cut designed to select objects within $1.1 < z < 1.6$. This RF classifier, like the one in Section 4.1, is trained on all magnitudes and color combinations from COSMOS2020.

The divisions we use for targeting were originally designed to select galaxies within the redshift range $1.05 < z < 1.55$; but in order to facilitate direct comparisons to statistics for the DESI ELG sample, we use the spectroscopic redshifts from the pilot sample to develop optimized cuts for selecting objects in the $1.1 < z < 1.6$ redshift range.

The cuts applied for the targeting of the pilot sample were shifted slightly from the RF optimized values to avoid regions that HSC photo-z's suggested were dominated by lower-redshift galaxies, resulting in a final set of selection cuts that were more exclusive in $r - i/i - y$ than the values optimized based on COSMOS2020 photometric redshifts and the classifier. The excluded portion of color space is included in our final color cuts, which were optimized based upon the spec-truth sample, reflecting the impact of the catastrophic failures for HSC photo-z's of ELGs that are illustrated in Figure 15.

We utilize a cutoff of 0.025 in the RF probability to distinguish the locations of low-redshift from high-redshift objects in color space; this choice is tuned based on the ROC curve to provide a high completeness for selecting high-z objects while maintaining a low degree of contamination. The final targeting cuts used for the pilot survey spectroscopic sample were as follows:

1. *g-band magnitude limits.* ($g_{\rm fiber} < 24.3$) **AND** ($g < 24$);
2. *r-band magnitude limits.* ($r_{\rm fiber} < 24.3$) **AND** ($r < 24$); and
3. *color cut.* ($i - y - 0.19 > r - i$) **AND** ($i - y > 0.35$).

All objects that fulfill either of the g- or r-band magnitude limits, and also fulfill the sample color cuts, are included in the

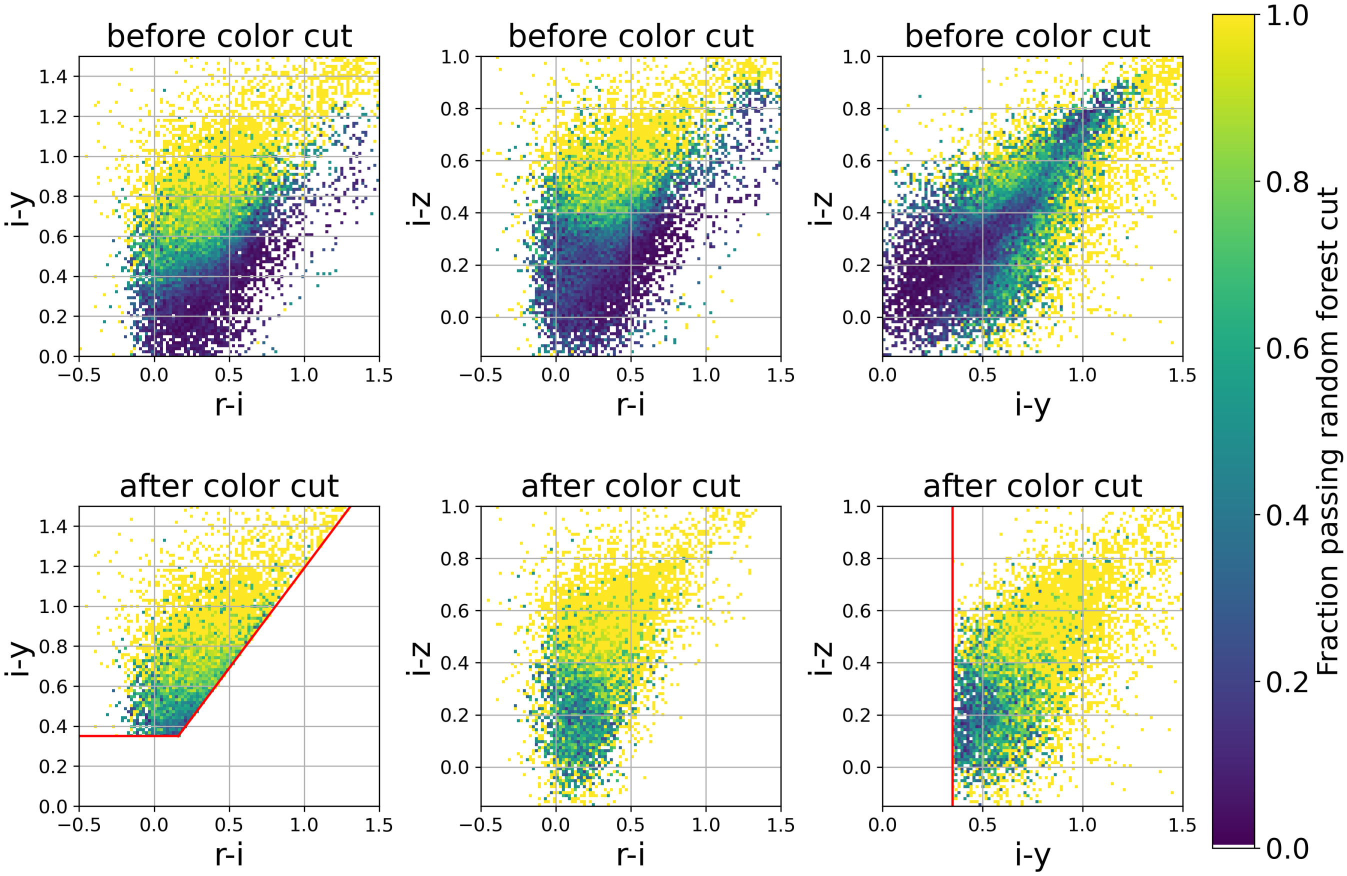

Figure 10. Color–color plots of $r - i/i - y/i - z$ color space, showing the fraction of objects that pass our RF probability $\geqslant 0.025$ cut before (top row of panels) or after (bottom panels) the simple color cuts used for targeting the pilot sample of potential high-redshift ELGs are applied. This figure includes only HSC wide galaxies with COSMOS2020 cross-matches. Guided by the RF, we are able to design simple color cuts that are effective at selecting objects within the redshift range of interest ($1.1 < z < 1.6$).

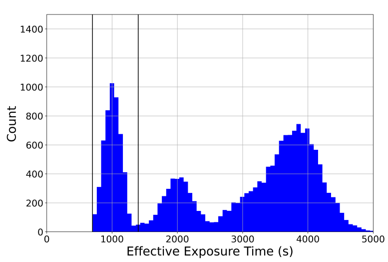

Figure 11. The exposure time distribution for the pilot sample. Only objects with effective exposure times in the range $700 < t < 1400$ s (indicated by the vertical black lines) are used for calculating redshift-measurement success rate ($f_{\rm reliable}$), whereas objects with longer exposures are included when calculating the redshift-measurement success rate ($f_{z\,=\,1.1\,-\,1.6}^{700\,<\,t\,<\,1400}$).

target sample. In total, spectra of 22,089 objects following these selection cuts are obtained in the pilot sample. Of those objects we obtain spectra for, 20,646 have reliable-redshift measurements.

In Figure 11, we show the distribution of effective exposure time (see Section 3) for the pilot sample galaxies. Only objects with exposure times in the range $700 < t_{\rm effective} < 1400$ s (between the solid black vertical lines on the figure) are used to calculate redshift-measurement success rates in order to enable fair comparisons to the DESI ELG sample, for which typical effective exposure times are $\simeq$1000 s. Objects with longer exposures are, however, included when calculating redshift distributions and related statistics in order to maximize sample sizes.

A.2. Results

Using the same optimization methods to fine-tune the final selection cuts as those described in Section 4.2, we are able to select a subset of the pilot survey sample that yielded values of $f_{\rm reliable}$, $f_{z\,=\,1.1\,-\,1.6}^{700\,<\,t\,<\,1400}$, and $\Sigma_{\rm yield}^{z\,=\,1.1\,-\,1.6}$ of 89%, 77%, and 1375 deg^{-2}, respectively. The final cuts obtained for our pilot survey sample are as follows:

1. $g_{\rm fiber} < 24.22$,
2. $i - y - 0.19 > r - i$,
3. $i - y > 0.37$, and
4. $i - z > 0.37$.

Comparing to the sample optimized based upon the spec-truth observations, the most noticeable difference is the lower redshift-range success rate (77% versus 84%) attained here. This difference is likely due to our inability to explore the $r - i/i - y$ color space as freely due to the stricter color cuts used for targeting (see the first panel of the bottom row in Figure 10). The final color cuts optimized based upon this sample are shown in Figure 12. These divisions are very similar to those obtained based upon the spec-truth sample; however, due to the restriction applied to the pilot sample

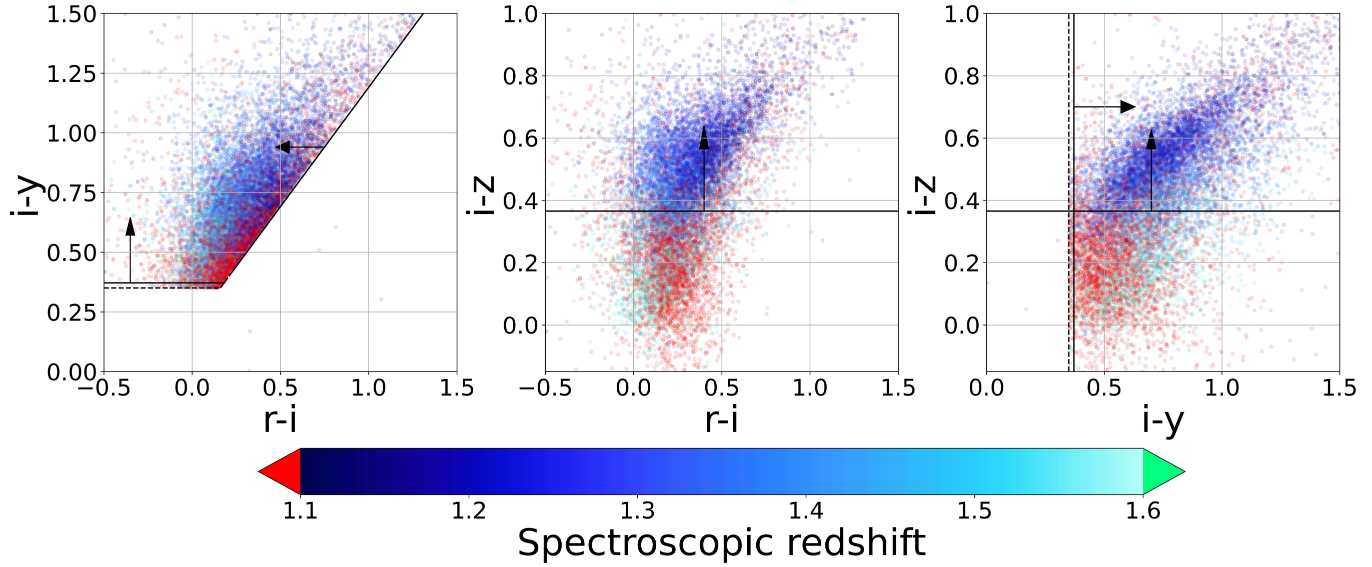

Figure 12. Color–color plots of galaxies with reliable redshifts from the high-z ELG sample in $r - i/i - y/i - z$ space, color-coded according to their spectroscopic redshift. Black dashed lines mark the color cuts used for targeting, and solid lines show the final cuts optimized based upon the spectroscopy. Adding an $i - z$ color cut is extremely effective at excluding $z < 1.1$ galaxies. The few objects beyond the limits of the dashed lines were due to inconsistencies between photometric catalogs.

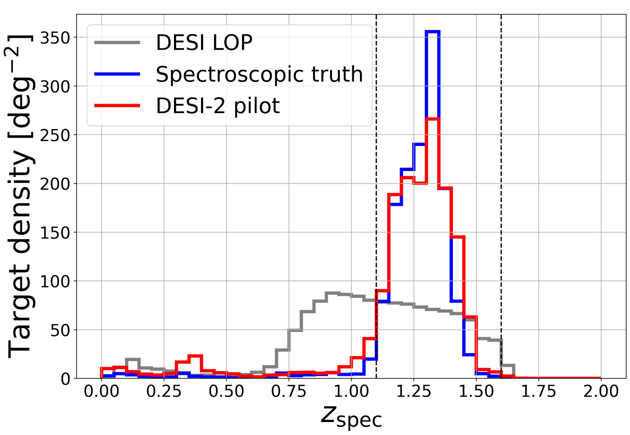

Figure 13. Redshift distributions (in galaxies per square degree per redshift bin) for DESI ELGs (gray), the high-z ELG sample optimized based upon the spec-truth observations (blue), and the high-z ELG sample optimized based upon the pilot sample spectroscopy (red). Unlike the DESI ELGs, both the pilot and spec-truth-optimized samples are almost entirely within the redshift range of greatest interest, $1.1 < z < 1.6$. Both samples are also much more efficient at selecting high-redshift ELGs than DESI ELGs, thanks to being able to exploit deeper photometry in more bands than were used for DESI.

targets based upon HSC photo-z predictions, it was not possible to test positive offsets to the $r - i/i - y$ diagonal line, limiting the degree of optimization possible.

In Figure 13 we compare the redshift distribution of the ELG sample optimized based on the pilot sample observations to both the DESI ELGs and the ELG sample optimized based upon the spec-truth spectra. As with the spec-truth-optimized sample, the pilot sample observations demonstrate that deeper multiband imaging makes it possible to significantly reduce low-redshift contamination and acquire a denser sample over the desired $1.1 < z < 1.6$ redshift range compared to DESI. Although it exhibits slightly more contamination at $z < 1.1$, the pilot sample optimization provides qualitatively similar results to the spec-truth selection. Combining the current DESI ELGs with samples designed with either of these sets of color cuts would allow for a future spectroscopic survey to provide significantly improved constraints on BAO cosmology at redshifts $1.1 < z < 1.6$.

Appendix B
Impact of Shallower Photometry

B.1. Methods

The HSC wide imaging is slightly deeper in some bands than the photometry that will be available early in the LSST survey. In order to test how being limited to shallower photometry might impact the selection of high-redshift ELGs, we have designed a set of selection cuts based upon artificially degraded *grizy* photometry from HSC wide.

First, we take the 5σ magnitude limits that LSST will achieve after the full 10 yr (Y10) dataset and degrade them to the expected values for a 2 yr (Y2) dataset, assuming that signal-to-noise scales as the square root of total exposure time as expected in the background-limited regime:

$$m_{\rm lim, LSST\ Y\ 2} = m_{\rm lim,\ LSST\ Y\ 10} + 1.25\log(2/10), \qquad (B1)$$

where $m_{\rm lim, LSST\ Y\ 2}$ and $m_{\rm lim, LSST\ Y\ 10}$ are the Y2 and Y10 5σ magnitude limits, respectively (F. B. Bianco et al. 2021). Using these predicted magnitude limits, we can calculate the expected errors for a particular object according to the equation:

$$\sigma_{\rm m} = \frac{1}{2\ln 10} \times 10^{\frac{m_{\rm HSC\ wide} - m_{\rm lim,\ LSST\ Y\ 2}}{2.5}}, \qquad (B2)$$

where $m_{\rm HSC\ wide}$ is the HSC wide magnitude for that object in a particular band and $m_{\rm lim, LSST\ Y\ 2}$ is the LSST Y2 5σ depth in the corresponding band. One can derive this equation via propagation of error from errors in flux into errors in magnitude, combined with the requirement that the fractional flux error must be one-fifth when $m_{\rm HSC\ wide} = m_{\rm lim, LSST\ Y\ 2}$. We

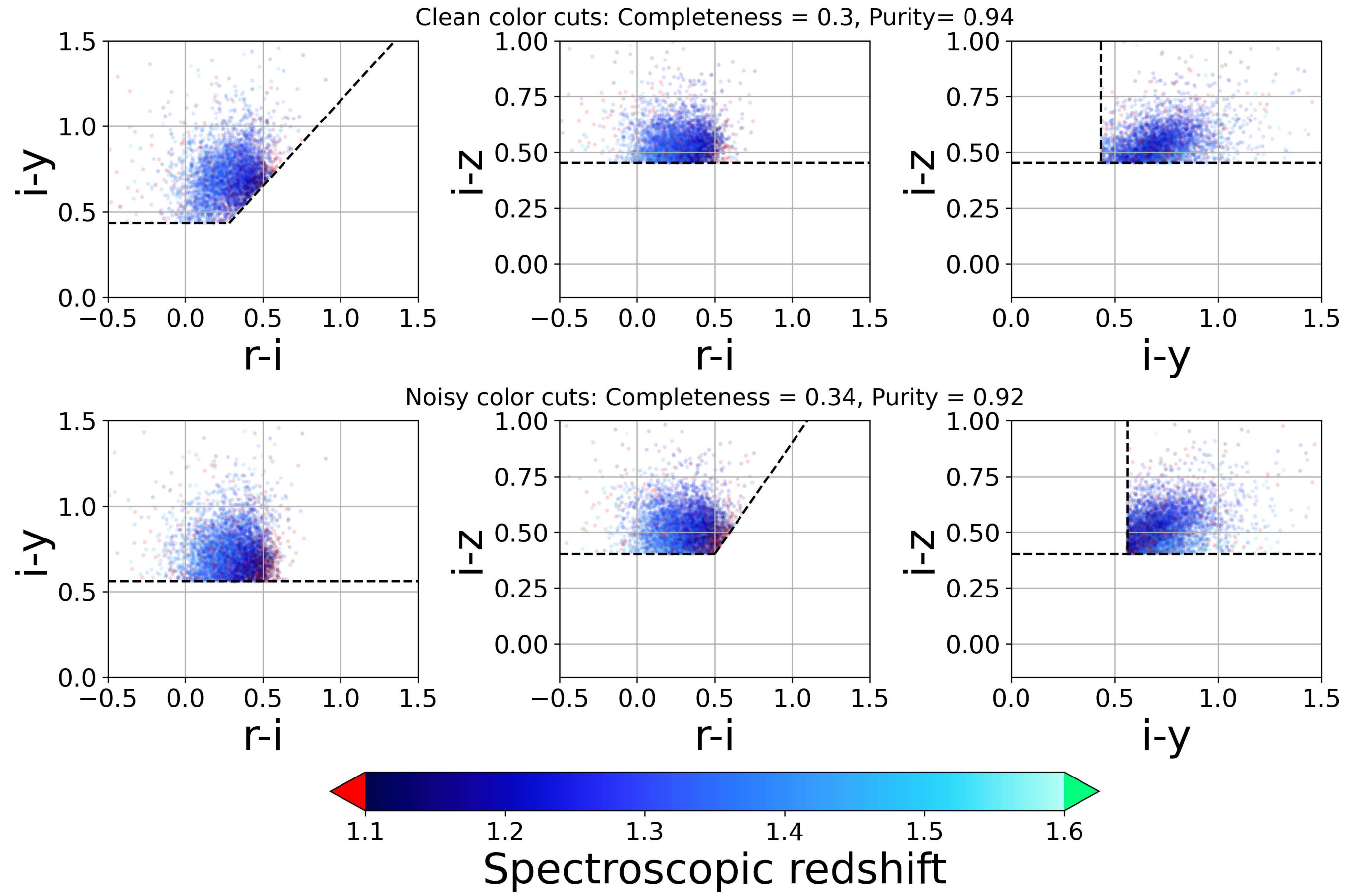

Figure 14. Color–color diagram of spec-truth galaxies color-coded by their $z_{\rm spec}$ with the positions of objects in color–color space plotted using either the original HSC wide photometry (top panel) or their positions after photometry is degraded based on LSST Y2 depths (bottom) after applying optimized color cuts. Despite a small decrease in purity, we are still able to obtain a very clean sample of galaxies that are predominantly in the redshift range $1.1 < z < 1.6$.

Table 2
5σ PSF Depths of HSC DR3 and LSST after 2 yr of Observations

5σ Depths	g	r	i	z	y
HSC DR3	26.5	26.5	26.2	25.2	24.4
LSST Y2	26.5	26.6	25.9	25.2	24.0

Note. The biggest difference between the two are for the y band, where HSC is deeper by 0.4 mag.

compare the 5σ depths for all bands of HSC DR3 to what is expected for LSST Y2 in Table 2. Dust can have a small effect on the effective depths, especially for the bluest bands, but we ignore that here.

We then generate random values from Gaussians with a mean of zero and a standard deviation of the appropriate $\sigma_{\rm m}$ value to each object's magnitudes, and add them to the original HSC magnitudes to obtain a set of noisier *grizy* measurements for all objects and bands. This gives us a set of magnitude values that scatter about the original HSC photometry at a level corresponding to Equation (B2). It is important to note that this procedure results in over-degraded photometry, since the HSC photometry that we apply expected LSST errors to has nonzero observational uncertainties, making our tests conservative.

B.2. Results

After obtaining this degraded photometry, we apply the same methods described in Section 4 to optimize selections for a sample of ELGs within the redshift range $1.1 < z < 1.6$ based upon the spec-truth redshifts. We compare these cuts optimized for noisier photometry to those we obtained before in Figure 14. After adding noise to the photometry, a diagonal $i - y/r - i$ cut became less ideal, and we went with a diagonal cut in $i - z/r - i$ instead. It is clear that it is still possible to obtain an efficient and dense selection of ELGs over the redshift range $1.1 < z < 1.6$ when limited to this noisier photometry. When optimizing based on the noisy photometry, we obtain values of redshift-measurement success rate ($f_{\rm reliable}$) of 89% (as compared to 89% for the sample described in Section 4.2), redshift-range success rate ($f_{z=1.1-1.6}^{700<t<1400}$) of 83% (versus 84%), a target density ($\Sigma_{\rm target}$) of 1656 deg^{-2} (compared to 1632 deg^{-2}), and net surface density yield ($\Sigma_{\rm yield}^{z=1.1-1.6}$) of 1366 deg^{-2} (versus 1372 deg^{-2}), respectively. Our results are qualitatively similar to those achieved with the nondegraded photometry while still greatly outperforming the DESI ELG sample, suggesting that LSST Y2 photometry would be sufficient to select ELG targets for a DESI-II program. The final cuts obtained for this noisier optimization are as follows:

1. $g_{\rm fiber} < 24.27$,
2. $i - z + 0.10 > r - i$,
3. $i - y > 0.56$, and
4. $i - z > 0.40$.

Appendix C
Testing Photometric Redshift Performance for High-z ELGs

In order to test the accuracy and performance of the COSMOS2020 photo-z's used to design our initial ELG selections, we can compare them to the spectroscopic redshifts of the same objects. We also test the HSC DNNz *grizy* photo-z's that are available for all of our objects (M. Tanaka et al. 2017; A. J. Nishizawa et al. 2020). In Figure 15, we show comparisons of the z_{spec} measurements for spec-truth objects with secure redshifts to either COSMOS2020 or HSC photo-z's, using both scatter plots and redshift histograms to compare.

Although it is only available for a fraction of the spec-truth sample due to the smaller sky area of the COSMOS field, the LePHARE photo-z's perform very well for this sample, having σ_{NMAD} and $f_{outliers}$ of 0.0084 and 2.3%, respectively. However, a handful of objects that are, in fact, at low redshift ($z \sim 0.25$) are instead placed much higher ($z \sim 2.5$). In contrast, the HSC grizy photo-z's exhibit a much higher catastrophic outlier rate ($f_{outliers} = 10.6\%$), particularly for objects that are in fact at $z \sim 0.1$. Similar results are reported in A. Raichoor et al. (2023). The larger scatter and outlier rate are presumably driven by the limited information about redshift available from grizy broadband photometry, though lack of faint, low-redshift galaxies in photo-z training sets may also play a role. The systematic failures of photo-z algorithms in relevant regimes highlight the importance of obtaining spectra when designing final selection criteria for high-redshift ELGs, as we have done in this work.

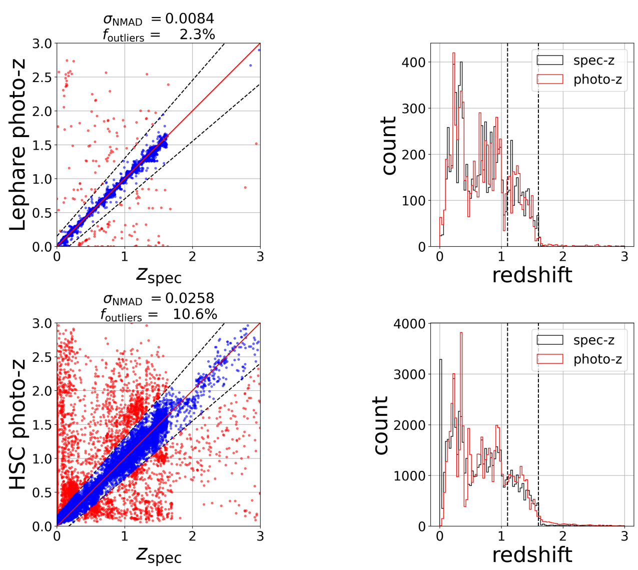

Figure 15. Comparison of COSMOS2020 (top row) or HSC (bottom row) photo-z's to the secure spectroscopic redshift measurements (z_{spec}) for the spec-truth sample. Here, $f_{outliers}$ is defined as the fraction with redshift difference $\frac{\Delta z}{1+z} > 0.15$. The limited information available in broadband *grizy* and the rarity of faint, low-redshift galaxies in training sets likely cause the much larger catastrophic outlier rates seen for the HSC photo-z's.

ORCID iDs

Yoquelbin Salcedo Hernandez https://orcid.org/0000-0001-9897-576X
Jeffrey A. Newman https://orcid.org/0000-0001-8684-2222
Brett H. Andrews https://orcid.org/0000-0001-8085-5890
B. Dey https://orcid.org/0000-0002-5665-7912
R. Zhou https://orcid.org/0000-0001-5381-4372
N. Sailer https://orcid.org/0000-0002-5333-8983
J. Aguilar https://orcid.org/0000-0003-0822-452X
S. Ahlen https://orcid.org/0000-0001-6098-7247
D. Bianchi https://orcid.org/0000-0001-9712-0006
D. Brooks https://orcid.org/0000-0002-8458-5047
F. J. Castander https://orcid.org/0000-0001-7316-4573
E. Chaussidon https://orcid.org/0000-0001-8996-4874
A. Cuceu https://orcid.org/0000-0002-2169-0595
A. de la Macorra https://orcid.org/0000-0002-1769-1640
A. Dey https://orcid.org/0000-0002-4928-4003
P. Doel https://orcid.org/0000-0002-6397-4457
S. Ferraro https://orcid.org/0000-0003-4992-7854
A. Font-Ribera https://orcid.org/0000-0002-3033-7312
J. E. Forero-Romero https://orcid.org/0000-0002-2890-3725
E. Gaztañaga https://orcid.org/0000-0001-9632-0815
S. Gontcho A Gontcho https://orcid.org/0000-0003-3142-233X
G. Gutierrez https://orcid.org/0000-0003-0825-0517
H. K. Herrera-Alcantar https://orcid.org/0000-0002-9136-9609
R. Joyce https://orcid.org/0000-0003-0201-5241
S. Juneau https://orcid.org/0000-0002-0000-2394
R. Kehoe https://orcid.org/0000-0002-7101-697X
D. Kirkby https://orcid.org/0000-0002-8828-5463
T. Kisner https://orcid.org/0000-0003-3510-7134
A. Kremin https://orcid.org/0000-0001-6356-7424
O. Lahav https://orcid.org/0000-0002-1134-9035
C. Lamman https://orcid.org/0000-0002-6731-9329
M. Landriau https://orcid.org/0000-0003-1838-8528
M. E. Levi https://orcid.org/0000-0003-1887-1018
M. Manera https://orcid.org/0000-0003-4962-8934
A. Meisner https://orcid.org/0000-0002-1125-7384
R. Miquel https://orcid.org/0000-0002-6610-4836
J. Moustakas https://orcid.org/0000-0002-2733-4559
S. Nadathur https://orcid.org/0000-0001-9070-3102
N. Palanque-Delabrouille https://orcid.org/0000-0003-3188-784X
W. J. Percival https://orcid.org/0000-0002-0644-5727
F. Prada https://orcid.org/0000-0001-7145-8674
I. Pérez-Ràfols https://orcid.org/0000-0001-6979-0125
A. Raichoor https://orcid.org/0000-0001-5999-7923
E. Sanchez https://orcid.org/0000-0002-9646-8198
D. Schlegel https://orcid.org/0000-0002-5042-5088
H. Seo https://orcid.org/0000-0002-6588-3508
J. Silber https://orcid.org/0000-0002-3461-0320
D. Sprayberry https://orcid.org/0000-0001-7583-6441
G. Tarlé https://orcid.org/0000-0003-1704-0781
C. Yèche https://orcid.org/0000-0001-5146-8533
H. Zou https://orcid.org/0000-0002-6684-3997

References

Abdul Karim, M., Aguilar, J., Ahlen, S., et al. 2025, PhRvD, 112, 083515
Adame, A. G., Aguilar, J., Ahlen, S., et al. 2025a, JCAP, 2025, 021
Adame, A. G., Aguilar, J., Ahlen, S., et al. 2025b, JCAP, 2025, 028
Aghamousa, A., et al. 2016, arXiv:1611.00036
Aihara, H., Arimoto, N., Armstrong, R., et al. 2017, PASJ, 70
Aihara, H., AlSayyad, Y., Ando, M., et al. 2019, PASJ, 71, 114
Aihara, H., AlSayyad, Y., Ando, M., et al. 2022, PASJ, 74, 247
Arnouts, S., & Ilbert, O. 2011, LePHARE: Photometric Analysis for Redshift Estimate, Astrophysics Source Code Library, ascl:1108.009
Astropy Collaboration, Price-Whelan, A. M., Lim, P. L., et al. 2022, ApJ, 935, 167
Astropy Collaboration, Price-Whelan, A. M., Sipőcz, B. M., et al. 2018, AJ, 156, 123
Astropy Collaboration, Robitaille, T. P., Tollerud, E. J., et al. 2013, A&A, 558, A33
Bianco, F. B., Ivezić, Ž., Jones, R. L., et al. 2021, ApJS, 258, 1
Brammer, G. B., van Dokkum, P. G., & Coppi, P. 2008, ApJ, 686, 1503
Breiman, L. 2001, MachL, 45, 5
Chaussidon, E., Yè che, C., Palanque-Delabrouille, N., et al. 2023, ApJ, 944, 107
Chen, S.-F., Vlah, Z., & White, M. 2019, JCAP, 09, 017
Coil, A. L., Newman, J. A., Croton, D., et al. 2008, ApJ, 672, 153
Cole, S., Percival, W. J., Peacock, J. A., et al. 2005, MNRAS, 362, 505
Dawson, K., Hearin, A., Heitmann, K., et al. 2022, arXiv:2203.07291
Dawson, K. S., Kneib, J.-P., Percival, W. J., et al. 2016, AJ, 151, 44
Dawson, K. S., Schlegel, D. J., Ahn, C. P., et al. 2013, AJ, 145, 10
DESI Collaboration, Abareshi, B., Aguilar, J., et al. 2022, AJ, 164, 207
DESI Collaboration, Abdul-Karim, M., Adame, A. G., et al. 2026, AJ, 171, 285
DESI Collaboration, Aghamousa, A., Aguilar, J.,, et al. 2016, arXiv:1611.00037
Dey, A., Schlegel, D. J., Lang, D., et al. 2019, AJ, 157, 168
Drinkwater, M. J., Jurek, R. J., Blake, C., et al. 2010, MNRAS, 401, 1429
Eisenstein, D. J., Annis, J., Gunn, J. E., et al. 2001, AJ, 122, 2267
Eisenstein, D. J., Zehavi, I., Hogg, D. W., et al. 2005, ApJ, 633, 560
Fawcett, T. 2006, PaReL, 27, 861
Flaugher, B., Diehl, H. T., Honscheid, K., et al. 2015, AJ, 150, 150
Guy, J., Bailey, S., Kremin, A., et al. 2023, AJ, 165, 144
Harris, C. R., Millman, K. J., van der Walt, S. J., et al. 2020, Natur, 585, 357
Hunter, J. D. 2007, CSE, 9, 90
Ivezić, Ž., Kahn, S. M., Tyson, J. A., et al. 2019, ApJ, 873, 111
König, G., Molnar, C., Bischl, B., & Grosse-Wentrup, M. 2020, arXiv:2007.08283
Kovesi, P. 2015, arXiv:1509.03700
Lang, D., Hogg, D. W., Mykytyn, D., et al. 2016, The Tractor: Probabilistic astronomical source detection and measurement, Astrophysics Source Code Library, ascl:1604.008
Miller, T. N., Doel, P., Gutierrez, G., et al. 2024, AJ, 168, 95
Myers, A. D., Palanque-Delabrouille, N., Prakash, A., et al. 2015, ApJS, 221, 27
Nishizawa, A. J., Hsieh, B.-C., Tanaka, M., & Takata, T. 2020, arXiv:2003.01511
Pedregosa, F., Varoquaux, G., Gramfort, A., et al. 2011, JMLR, 12, 2825
Poppett, C., Tyas, L., Aguilar, J., et al. 2024, AJ, 168, 245
Prakash, A., Licquia, T. C., Newman, J. A., et al. 2016, ApJS, 224, 34
Raichoor, A., Moustakas, J., Newman, J. A., et al. 2023, AJ, 165, 126
Sailer, N., Castorina, E., Ferraro, S., & White, M. 2021, JCAP, 12, 049
Sailer, N., Kim, J., Ferraro, S., et al. 2025, JCAP, 2025, 008
Sawicki, M., Arnouts, S., Huang, J., et al. 2019, MNRAS, 489, 5202
Schlafly, E. F., Kirkby, D., Schlegel, D. J., et al. 2023, AJ, 166, 259
Schlegel, D. J., Ferraro, S., Aldering, G., et al. 2022, arXiv:2209.03585
Schlegel, D. J., Finkbeiner, D. P., & Davis, M. 1998, ApJ, 500, 525
Schreiber, N. M. F., & Wuyts, S. 2020, ARA&A, 58, 661
Seo, H.-J., & Eisenstein, D. J. 2007, ApJ, 665, 14
Tanaka, M., Coupon, J., Hsieh, B.-C., et al. 2017, PASJ, 70, S9
The pandas development team 2020, pandas-dev/pandas: Pandas, v3.0.3, Zenodo, doi: 10.5281/zenodo.3509134
Virtanen, P., Gommers, R., Oliphant, T. E., et al. 2020, NatMe, 17, 261
Weaver, J. R., Kauffmann, O. B., Ilbert, O., et al. 2022, ApJS, 258, 11
Weinberg, D. H., Mortonson, M. J., Eisenstein, D. J., et al. 2013, PhR, 530, 87
York, D. G., Adelman, J., Anderson, J. E., Jr., et al. 2000, AJ, 120, 1579
Zhou, R., Dey, B., Newman, J. A., et al. 2023a, AJ, 165, 58
Zhou, R., Ferraro, S., White, M., et al. 2023b, JCAP, 2023, 097